CrossMark

RESEARCH ARTICLE

Simultaneous three-component velocity measurements in a swirl-stabilized flame

Raimund Schlüßler[1] · Mike Bermuske[1] · Jürgen Czarske[1] · Andreas Fischer[1]

Abstract Modern gas turbines are operated with lean fuel mixtures causing instabilities of the heat release and, by means of a thermoacoustic coupling, oscillations of the flow velocity within the flame. Since these oscillations can reduce the combustion efficiency, a better understanding of their formation mechanism and spatial origin is necessary. Therefore, simultaneous, three-component (3C) velocity measurements with high measurement rate are required. The Doppler global velocimetry with laser frequency modulation (FM-DGV) achieves measurement rates up to 100 kHz and was successfully applied for measurements in flames, but does not provide simultaneous 3C velocity data. In order to overcome this drawback, the FM-DGV is extended to allow simultaneous 3C measurements. The functionality is demonstrated by measurements within a swirl-stabilized flame. In combination with time-resolved measurements of the sound pressure and chemiluminescence emission, the spatial origin of the sound pressure emission in the acoustic far-field is identified as flow velocity and heat release oscillations in the acoustic near-field of the flame. Hence, a deeper insight into the thermoacoustic coupling can be achieved.

✉ Raimund Schlüßler
  raimund.schluessler@tu-dresden.de

  Mike Bermuske
  mike.bermuske@tu-dresden.de

  Jürgen Czarske
  juergen.czarske@tu-dresden.de

  Andreas Fischer
  andreas.fischer2@tu-dresden.de

[1] Laboratory for Measurement and Testing Techniques, Technische Universität Dresden, Helmholtzstr. 18, 01062 Dresden, Germany

1 Introduction

1.1 Motivation

In order to reduce the emission of mono-nitrogen oxides (NO_x) and carbon monoxide (CO) in modern gas turbines, these systems are operated with low combustion temperatures by using very lean fuel mixtures. The reduced fuel supply can lead to combustion instabilities causing fluctuations of the local heat release rate within the flame (Alavandi and Agrawal 2005; Candel et al. 2014; Richards et al. 2001). By means of thermoacoustic coupling, large pressure oscillations can result, which reduce the combustion efficiency or even damage the combustor itself due to induced vibrations. In order to improve the properties of gas turbine combustors, a deeper understanding of the formation mechanism and spatial origin of this coupling within the flame is necessary. Therefore, a correlation between the flow velocity in the acoustic near-field and the sound pressure in the far-field can be performed, allowing to analyze the origin of the sound pressure emission within the flame (Henning et al. 2008). In case of periodic oscillations with distinct frequencies, this is similar to locating the flame region with the highest amplitudes of flow velocity oscillations at the characteristic frequency of the sound emission. Hence, measurements of the sound emission in the acoustic far-field in combination with time-resolved measurements of the flow velocity in the near-field are required. Additional measurements of the heat release rate within the flame, e.g., by chemiluminescence measurements of OH* and CH* emissions or by OH planar laser-induced fluorescence (OH-PLIF) measurements (Giezendanner et al. 2003; Boxx et al. 2013; Gounder et al. 2014; Yilmaz et al. 2010), further allow to analyze the thermoacoustic coupling. Also,

laser interferometric vibrometry (LIV) can be applied to directly detect density fluctuations within the flame related to the heat release rate (Fischer et al. 2013a; Giuliani et al. 2006, 2010). However, due to the complex flow behavior of swirl-stabilized flames, flow velocity measurements in these kinds of flames are a challenging task. For these measurements, a high measurement rate in the range of several kilohertz is typically required for the temporal analysis of the flow, e.g., to calculate the flow velocity spectra for turbulence analysis (Fischer et al. 2009) or to measure the acoustic particle velocity in the entire audible range (Haufe et al. 2013). Furthermore, a simultaneous acquisition of all three velocity components (3C) is desired, e.g., to analyze the flow velocity oscillations of all three velocity components in Cartesian coordinates.

1.2 State of the art

In order to acquire the flow velocity for swirl-stabilized combustors, various measurement techniques are available. Early flow velocity measurements related to swirled combustion were conducted using hot-wire anemometers, which only allowed to measure the flow velocity under cold conditions without a flame (Syred et al. 1971). First simultaneous three-component velocity measurements in hot reactive flows were realized using laser Doppler anemometry (LDA) (Baker et al. 1975; Self and Whitelaw 1976). However, since LDA does not provide continuous velocity data, this is not ideal for calculating the velocity spectra. An extensive review of this early work regarding swirled combustion can be found in (Syred and Beér 1974; Lilley 1977).

In the recent research, the most common measurement principle for flow velocity measurements in flames is the particle image velocimetry (PIV) (Sadanandan et al. 2009). The basic realization of this technique provides measurement rates in the range of several hertz and is therefore not able to directly resolve fast velocity oscillations in the range of several kilohertz. Fast oscillations could be resolved by phase locking onto a single frequency, though information about oscillations with other frequencies is lost, which can be problematic for analyzing the precessing vortex core (Syred 2011). To overcome this problem, high-speed PIV systems are used, which provide sufficient measurement rates (Meadows and Agrawal 2014). However, they do not allow three-component flow velocity measurement. For this reason, stereoscopic high-speed PIV systems are applied, achieving measurement rates up to 10 kHz (Boxx et al. 2012, 2013; Stöhr et al. 2012). Even higher measurement rates up to 100 kHz have been achieved using a Doppler global velocimeter with laser frequency modulation (FM-DGV), giving access to the entire audible range. Also, DGV techniques are known to be less susceptible to

fluctuations of the refractive index, e.g., due to heat fluctuations in the imaging path as they are likely to appear for measurements in hot gases (Schlüßler et al. 2014). In Fischer et al. (2013a), FM-DGV was successfully introduced for three-component flow velocity measurements in flames. However, each component was measured successively, and thus, an analysis of, for example, flow velocity oscillations in Cartesian coordinates was not yet possible. To overcome this limitation, we present an enhanced, simultaneous three-component FM-DGV system (3C FM-DGV), enabling the localization of the sound pressure emission within the flame.

1.3 Aim and structure

In the present article, a novel, simultaneous three-component FM-DGV system capable of flow velocity measurements in swirl-stabilized flames with high measurement rate is presented. The applicability of the system for combustion research is demonstrated by flow velocity measurements at a swirl-stabilized burner with variable geometry, which allowed the localization of flow velocity oscillations within the flame. The results are combined with sound pressure measurements in the far-field of the burner. Hence, the source of the sound emission of the combustor can be attributed to localized flow velocity oscillations within the flame. Furthermore, chemiluminescence measurements are performed to analyze the thermoacoustic coupling.

First, we introduce and characterize the novel 3C FM-DGV system in Sect. 2. Subsequently, the experimental setup including the used swirl burner and the applied measurement techniques are described in Sect. 3. The measurement results acquired by 3C FM-DGV, microphone and chemiluminescence measurements are presented and discussed in Sect. 4. Finally, the conclusions are summarized and an outlook is given in Sect. 5.

2 Measurement technique development

2.1 Measurement principle

The measurement principle of FM-DGV is based on evaluating the Doppler frequency shift

$$f_{D,\mathbf{o}_m,\mathbf{i}_n} = \frac{|\mathbf{o}_m - \mathbf{i}_n|}{\lambda} \cdot v_{\mathbf{o}_m,\mathbf{i}_n} \quad \text{with} \quad v_{\mathbf{o}_m,\mathbf{i}_n} = \frac{(\mathbf{o}_m - \mathbf{i}_n)}{|\mathbf{o}_m - \mathbf{i}_n|} \cdot \mathbf{v}_p \quad (1)$$

of scattered light due to the velocity $\mathbf{v}_p$ of a tracer particle observed from the direction $\mathbf{o}_m$ and illuminated from the direction $\mathbf{i}_n$ using a narrow linewidth laser light source with the wavelength λ as depicted in Fig. 1a. Here, m indexes the observation directions and n indexes the illumination directions. Note that $\mathbf{o}_m$ and $\mathbf{i}_n$ are unit vectors, i.e.,
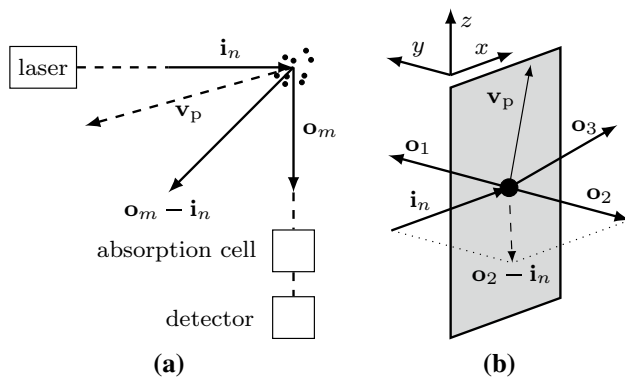
Fig. 1 a Measurement principle of FM-DGV and **b** Example arrangement of the illumination direction **i** and observation directions $\mathbf{o}_m, m = 1, 2, 3$

$|\mathbf{o}_m| = |\mathbf{i}_n| = 1$. In order to measure the Doppler frequency f_D, the frequency shift of the scattered light is converted to an intensity variation by means of a molecular absorption cell. The intensity variation behind the cell is finally measured using a photosensitive device. Regarding FM-DGV, the laser frequency is sinusoidally modulated with the modulation frequency f_m, and the quotient

$$q_{\mathbf{o}_m,\mathbf{i}_n}(f_{D,\mathbf{o}_m,\mathbf{i}_n}) = \frac{A_1(f_{D,\mathbf{o}_m,\mathbf{i}_n})}{A_2(f_{D,\mathbf{o}_m,\mathbf{i}_n})} \quad (2)$$

of the amplitudes A_1 and A_2 of the first and second harmonic of the intensity signal is evaluated. The quotient q is a measure for the Doppler frequency independent of the mean scattered light power, because the mean scattered light power affects both amplitudes A_1 and A_2 as a factor and is eliminated by the formation of the quotient (Fischer et al. 2007; Müller et al. 2007). The relation between the measured quotient q and the desired Doppler frequency f_D, respectively the component $v_{\mathbf{o}_m,\mathbf{i}_n}$ of the flow velocity vector, is determined by a calibration.

According to Eq. (1), the velocity component $v_{\mathbf{o}_m,\mathbf{i}_n}$ along the direction $\mathbf{o}_m - \mathbf{i}_n$ is measured. Hence, with one combination of illumination and observation directions only one component of the flow velocity vector $\mathbf{v}_p$ can be measured. In order to conduct a measurement of all three velocity components, the total number of different illumination and observation directions must be at least four. Hereby, every combination of illumination and observation directions is possible, e.g., three illumination directions and one observation direction (Fischer et al. 2011; Röhle and Willert 2001) or one illumination direction and three observation directions (Charrett and Tatam 2006; Komine et al. 1991; Meyers 1995). However, the spatial arrangement of these directions has to be chosen in order to obtain a basis of the velocity vector space and to maximize the sensitivity of the measurement system (Charrett et al. 2007).

With DGV, it is in general not possible to directly acquire an orthonormal basis (e.g., Cartesian coordinates) of the velocity vector space, as the optical access is normally limited. Hence, a coordinate transformation between the measured velocity **v** with the components $v_{\mathbf{o}_m,\mathbf{i}_n}$ and the desired velocity $\mathbf{v}_p$ of the flow is necessary.

Here, one illumination direction ($n = 1$) and three observation directions ($m = 1, 2, 3$) are used, because this setup requires the lowest technical effort. The observation and illumination alignment used for the measurements within the flame is depicted in Fig. 1b. The respective coordinate transformation for this setup reads

$$\mathbf{v}_p = M^{-1} \cdot (v_{\mathbf{o}_1,\mathbf{i}_1}, v_{\mathbf{o}_2,\mathbf{i}_1}, v_{\mathbf{o}_3,\mathbf{i}_1})^T \quad (3)$$

with the transform matrix

$$M = \begin{pmatrix} \frac{(\mathbf{o}_1 - \mathbf{i}_1)^T}{|\mathbf{o}_1 - \mathbf{i}_1|} \\ \frac{(\mathbf{o}_2 - \mathbf{i}_1)^T}{|\mathbf{o}_2 - \mathbf{i}_1|} \\ \frac{(\mathbf{o}_3 - \mathbf{i}_1)^T}{|\mathbf{o}_3 - \mathbf{i}_1|} \end{pmatrix}. \quad (4)$$

2.2 Measurement setup

The 3C FM-DGV system setup applied in this paper is based on the 1C FM-DGV system described in Fischer et al. (2013b). It consists of a master oscillator power amplifier (MOPA) laser system with about 1W output power at a wavelength of 895 nm. The modulation frequency f_m of the laser center frequency amounts to 100 kHz. Hence, the maximum measurement rate is 100 kHz, which here also means a high temporal resolution of 10 μs (Fischer et al. 2008a). The molecular absorption cell is filled with cesium gas. In order to keep the transmission constant, the absorption cell is temperature stabilized. For light detection, 24 avalanche photo diodes (APD) with a minimal noise equivalent power of $31\,\mathrm{fW}/\sqrt{\mathrm{Hz}}$ and a responsivity of 1.71×10^8 V/W are used (Fischer et al. 2009). The data acquisition is realized using a digitizer system with 26 channels and 14 bit resolution. In order to allow simultaneous measurements of all three flow velocity components, the system is extended to three observation directions.

For that purpose, two different approaches are possible: applying fiber bundles in order to guide the scattered light from the three different observation directions through a single, common absorption cell or observe the measurement volume directly through three distinct cells. Using a common absorption cell would reduce the calibration effort and potentially decrease the measurement uncertainty due to temperature variations within the cells. This could be realized using a matrix detector, i.e., a camera (Charrett et al. 2007). However, in combination with fiber-coupled

APD units used here, a common absorption cell would demand a fiber-to-fiber mapping, which would increase the alignment effort and reduce the scattered light power and is therefore not preferable. Hence, three distinct cesium absorption cells are used.

In difference to the former setup, the cells feature a larger diameter of 50 mm. As a result, a two times higher numerical aperture is achieved, which increases the received scattered light power by a factor of four. Since three observation directions, i.e., three APD units, are necessary for each measurement point, the 24 available APD units result in eight measurement points. The scattered light is mapped through the absorption cells onto fiber bundles, which guide the light to the APD units. The fiber bundles consist of eight fibers each with a diameter of 400 μm and a clearance of 440 μm.

2.3 Calibration and characterization

In this section, the calibration of the 3C measurement system is described, and the achievable measurement uncertainty with respect to the mean scattered light power is analyzed.

2.3.1 Calibration

In order to acquire the relations between the measured quotients $q_{\mathbf{o}_m,\mathbf{i}_1}$ and the velocities $v_{\mathbf{o}_m,\mathbf{i}_1}$ to be measured ($m = 1, 2, 3$), a calibration is performed. The arrangement of the calibration measurement is depicted in Fig. 2a with $\gamma = 35°$. A rotating carbon-fiber-reinforced polymer disk is used as calibration object. The front side of the disk is illuminated through a cylindrical lens at a given radius under a small angle of 4° to the disk surface. Knowing the rotational frequency and the spatial arrangement of the disk, the velocity $\mathbf{v}_p$ of each point of the disk can be calculated. Using $(v_{\mathbf{o}_1,\mathbf{i}_1}, v_{\mathbf{o}_2,\mathbf{i}_1}, v_{\mathbf{o}_3,\mathbf{i}_1})^T = M \cdot \mathbf{v}_p$ [c.p. Eq. (3)] with the appropriate transform matrix M yields the measured velocities $v_{\mathbf{o}_m,\mathbf{i}_1}$ for each observation direction and measurement point.

The calibration of all three observation units is performed simultaneously. As an example for a calibration, the measured quotients $q_{\mathbf{o}_m,\mathbf{i}_1}$ of the first measurement point are plotted against the observed velocities $v_{\mathbf{o}_m,\mathbf{i}_1}$ ($m = 1, 2, 3$) in Fig. 2b. The measured quotient shows a monotonous increase with increasing velocity.

2.3.2 Measurement uncertainty

In the following, the measurement uncertainty of the 3C FM-DGV system is discussed. Note that systematic errors are not considered here, because the main concern is to measure velocity oscillations where systematic errors do not contribute to the measurement uncertainty. In order to estimate the random error $\sigma(\mathbf{v}_p) = (\sigma(v_x), \sigma(v_y), \sigma(v_z))^T$ of the simultaneous 3C measurement system, the transform matrix M and the measurement uncertainties $\sigma(v_{\mathbf{o}_m,\mathbf{i}_1})$ of each component have to be known. By means of propagation of uncertainty using Eq. (3), it follows

$$\sigma(\mathbf{v}_p) \odot \sigma(\mathbf{v}_p) = \left(M^{-1} \odot M^{-1}\right) \cdot (\sigma(\mathbf{v}) \odot \sigma(\mathbf{v})) \quad \text{with}$$
$$\sigma(\mathbf{v}) = (\sigma(v_{\mathbf{o}_1,\mathbf{i}_1}), \sigma(v_{\mathbf{o}_2,\mathbf{i}_1}), \sigma(v_{\mathbf{o}_3,\mathbf{i}_1}))^T \tag{5}$$

and $\odot$ denoting the entrywise multiplication (Hadamard product). The transform matrix M and the inverse M^{-1} for the alignment of the observation and illumination units used for the measurements at the swirl burner (shown in Fig. 5) read
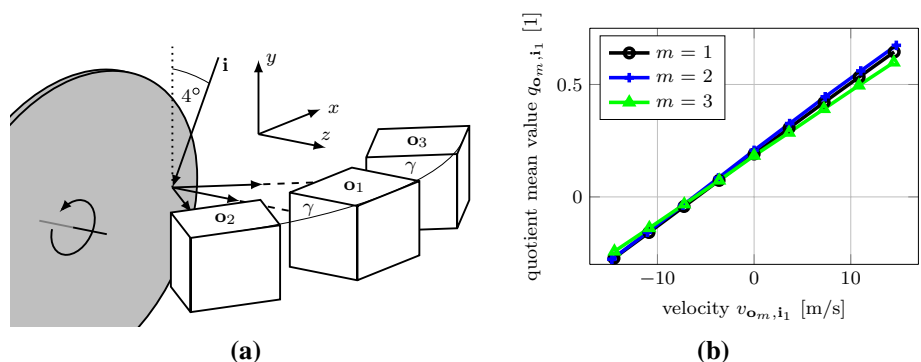
$$M = \frac{1}{\sqrt{2}} \cdot \begin{pmatrix} -1 & 1 & 0 \\ -1 & -1 & 0 \\ -1 & -\cos\beta & \sin\beta \end{pmatrix} \quad \text{and}$$
$$M^{-1} = \frac{1}{\sqrt{2}} \cdot \begin{pmatrix} -1 & -1 & 0 \\ 1 & -1 & 0 \\ \frac{\cos\beta-1}{\sin\beta} & \frac{-\cos\beta-1}{\sin\beta} & \frac{2}{\sin\beta} \end{pmatrix}. \tag{6}$$

with $\beta = 35°$. Hence, it follows from Eq. (5)

$$\sigma(v_x) = \sqrt{0.5 \cdot \sigma^2(v_{\mathbf{o}_1,\mathbf{i}_1}) + 0.5 \cdot \sigma^2(v_{\mathbf{o}_2,\mathbf{i}_1})} \tag{7}$$

Fig. 2 **a** Calibration setup for the 3C FM-DGV system and **b** the calibration curves for the first measurement point

(a)   **(b)**

$$\sigma(v_y) = \sqrt{0.5 \cdot \sigma^2(v_{\mathbf{o_1,i_1}}) + 0.5 \cdot \sigma^2(v_{\mathbf{o_2,i_1}})} \tag{8}$$

$$\sigma(v_z)$$
$$= \sqrt{0.050 \cdot \sigma^2(v_{\mathbf{o_1,i_1}}) + 5.030 \cdot \sigma^2(v_{\mathbf{o_2,i_1}}) + 6.079 \cdot \sigma^2(v_{\mathbf{o_3,i_1}})}. \tag{9}$$

According to (Fischer et al. 2008b, 2013b), the random error $\sigma(v_{\mathbf{o_m,i_1}})$ of one component can be estimated by

$$\sigma(v_{\mathbf{o_m,i_n}}) \approx \frac{1}{\sqrt{T/\mathrm{s}}} \cdot \sqrt{c_0^2 + \frac{c_1^2}{P/\mathrm{nW}} + \frac{c_2^2}{(P/\mathrm{nW})^2}} \tag{10}$$

with T as the measurement time and P as the mean detected scattered light power. The coefficients c_i characterize the contributions of three different error sources:

- The first coefficient c_0 denominates the error sources independent of the detected scattered light power, e.g., the laser center frequency stabilization,
- the second coefficient c_1 is related to the shot noise and possible avalanche excess noise and
- the third coefficient c_2 describes the contribution of the thermal noise and the dark current noise.

In order to determine the coefficients c_0, c_1 and c_2, velocity measurements for different scattered light powers are performed. The random error, i.e., the standard deviation of the flow velocity, is normalized to the time resolution T. The scattered light power is measured by a photodetector with given responsivity.

The standard deviation of the velocity is plotted against the mean detected scattered light power in Fig. 3. Note that the standard deviation is normalized to the temporal resolution T. The continuous line shows the fitted theoretical curve according to Eq. (10). The determined coefficients c_i are given in Table 1. Assuming a temporal resolution of 1 s, a measurement uncertainty of 4.4×10^{-2} m/s results
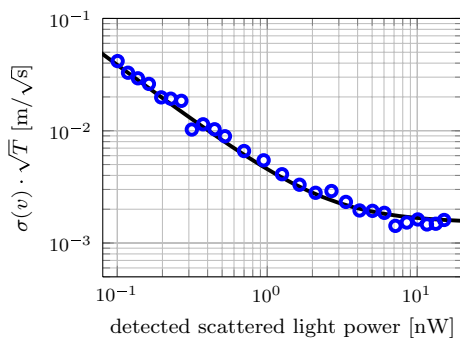
Fig. 3 Normalized velocity standard deviation of the 3C FM-DGV system with respect to the scattered light power. The standard deviation is normalized to the temporal resolution T, and the continuous line shows the theoretical curve fitting according to Eq. (10)

for low scattered light powers of 0.1 nW. The measurement uncertainty is reduced down to 1.8×10^{-3} m/s with an increased scattered light power of 10 nW. In this experiment, velocity values with a mean scattered light power below 0.2 nW are discarded due to the increased uncertainty.

In conclusion, according to Eqs. (7)–(9) the minimal possible random errors for the x, y and z direction given the alignment used at the swirl burner amount to $\sigma(v_x) = \sigma(v_y) = \sigma(v)$ and $\sigma(v_z) = 3.341 \cdot \sigma(v)$, with $\sigma(v) = 1.8 \times 10^{-3}$ m/s to 2×10^{-2} m/s. Note that this estimation is the lower limit for the random errors of the velocity measurement and the actual measurement uncertainty can be increased, e.g., due to turbulence. Also, these values are valid in case that all observation directions detect the same mean scattered light power and neglecting further error contributions as flame glow.

3 Experimental setup

3.1 Swirl-stabilized burner

In this section, the used swirl-stabilized burner is presented. First, the mechanical setup is illustrated; subsequently, the used flame types are characterized.
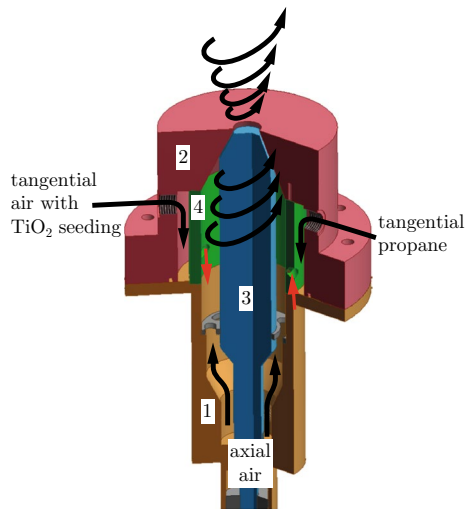
3.1.1 Mechanical setup

The burner used in this paper is schematically shown in Fig. 4. Its design is derived from the swirl burner described in (Fischer et al. 2013a; Giuliani et al. 2012) and features a variable geometry. The burner mainly consists of four parts: a lower (1) and an upper housing (2), a movable central piston (3) and an inner bushing (4). The air and the propane used as fuel are supplied by eight connectors into a mixing chamber within the upper housing. The swirl of the flow is passively introduced by the inner bushing shown in green. It features four tangential inlets, by which the mixed gas is tangentially conducted into the center of the burner, as indicated by the red arrows in Fig. 4. The outlet of the burner has a diameter of 15 mm, and its cross section can be adjusted by the central piston. The mass flow of the tangential air is controlled by a mass flow controller of the type 8626 from the company Bürkert. Axial air is not supplied.

3.1.2 Flame characterization

In order to demonstrate the applicability of the FM-DGV system for measurements at a swirled flame, two operational points are used: an operational point with medium sound pressure oscillations, subsequently denoted as the

Table 1 Error contributions for the 3C FM-DGV system

c_0 (m/s)	c_1 (m/s)	c_2 (m/s)
0.0015	0.002	0.0038

Table 2 Parameters for the chosen operational points of the burner

Operation point	Equivalence ratio (1)	Exit velocity (m/s)	Swirl number (1)	Thermal power (W)	Air mass flow (kg/h)
"Design point"	0.71	8.3	0.38	700	1.6
"Noisy flame"	0.64	7.7	0.47	700	1.8

Fig. 4 Schematic diagram of the swirl-stabilized burner with premixed flame

Fig. 5 Measurement setup of the 3C FM-DGV system

"design point," and an operational point with high sound pressure oscillations subsequently denoted as "noisy flame." For both flame types, the mass flow of propane is set to 37 g/h, which results in an emitted thermal power of approximately 700 W. For the design point and the noisy flame air, mass flows of 1.6 and 1.8 kg/h are used, according to an equivalence ratio of 0.71 and 0.64, respectively. As an important value for characterizing swirled flames, the swirl number is calculated as specified in Candel et al. (2014) from the measured tangential and axial velocity at the burner exit presented in Sect. 4 and amounts to 0.38 and 0.47, respectively. Hence, both flame types are considered to be in low-swirl condition. All characteristic parameters of both operational points are listed in Table 2.
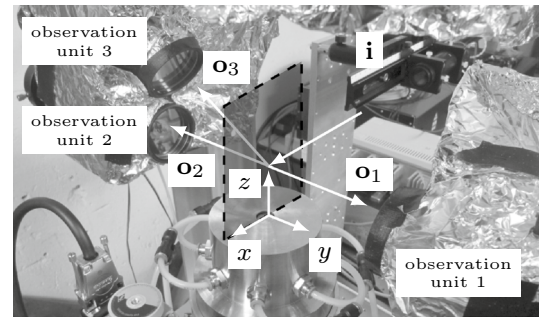
3.2 Applied measurement techniques

3.2.1 Flow velocity measurement

In order to acquire the flow velocity, the 3C FM-DGV system is used. The respective measurement setup is shown in Fig. 5. The observation directions $\mathbf{o}_1$ and $\mathbf{o}_2$ lie in opposite direction within the y–z plane perpendicular to the illumination direction $\mathbf{i}$. The observation direction $\mathbf{o}_3$ is tilted by an angle $\beta = 35°$ with respect to the x–y plane. As imaging optics, two achromatic doublet lenses with a focal length of 150 mm in front of the absorption cell and a focal length of

75 mm behind the cell are used. This leads to a working distance of 150 mm and a reproduction scale of 1:2. Hence, the spatial resolution in the x–z plane amounts to 800 μm due to the fiber end diameter of 400 μm. The spatial resolution in y direction is given by the illumination beam diameter of approximately 600 μm. In order to align all three fiber bundles to each other, light from a probe laser is coupled to the detector side end of the fiber, and the fiber ends are imaged into the measurement volume. Hence, the lateral arrangement of the fibers can be observed and adjusted. The accuracy of this alignment procedure is estimated to be 100 μm. Due to the margin between two adjacent fibers of 40 μm in the image space, i.e., 80 μm in the object space, a maximum overlap of 20 μm is expected. Considering the circular fiber end face, this results in a negligible cross talk of below 1 %.

The measurement points are arranged along a line in x direction. In order to measure the flow velocity within the x–z plane, the burner is traversed in x and z direction in steps of 900 μm and 7.2 mm, respectively, using a three-axis traversing system. Hence, a 2D3C velocity measurement is performed by measuring simultaneously all three components and successively two dimensions of the flow.

Ten acquisitions with a modulation frequency, i.e., measurement rate of 100 kHz, are performed with a duration of 1 s each, yielding a total measurement duration of 10 s for each measurement point. For data reduction purposes, 10 measurement values are averaged, resulting in a measurement rate of 10 kHz, which is sufficient to resolve the sound pressure oscillations revealed by the microphone measurements.

Fig. 6 Mean flow velocity in the *x–z* plane for **a** the design point and **b** the noisy flame. The measurement duration amounts to 10 s. The vectors depict the inplane components v_x and v_z, the color represents the out-of-plane component v_y
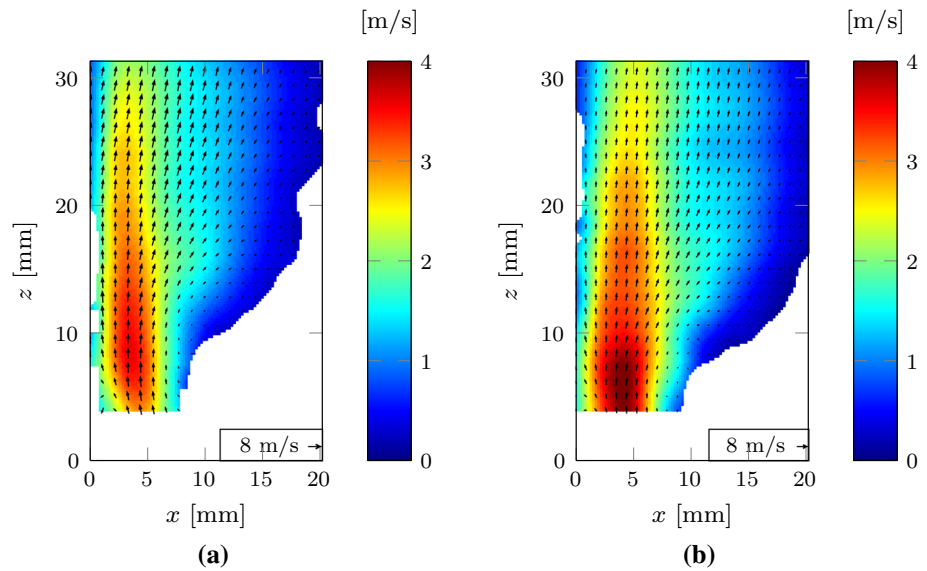
As tracer particles, titanium dioxide (TiO_2) particles with an average size of 0.4 µm are used. Due to agglomeration within the seeding generator, the effective particle size varies from 0.5 to 1 µm (Fischer et al. 2013a). In order to estimate the number of sampled particles per measurement value, the mean particle count within the measurement volume has to be known. In fact, at least one particle has to be within the measurement volume at all times during the complete measurement duration in order to scatter light into the observation aperture. Since a continuous scattered light signal was acquired, the mean particle count is expected to be significantly higher; a mean particle count of approximately 10 particles appears reasonable. Given the measurement volume of $0.38\,\text{mm}^3$, this results in an estimated particle density of $2.6 \times 10^{10}\,\text{m}^{-3}$, which is consistent with estimations performed for Di-Ethyl-Hexyl-Sebacat seeding (Fischer et al. 2011). As subject to the flow velocity, a sampled particle count of 10 up to 23 particles for one velocity value with a temporal resolution of 100 µs results for the measured particle velocity of 0–10 m/s, respectively. Hence, in order to obtain one velocity value, the velocities of multiple particles are averaged, weighted with the scattered light power of each particle (Fischer et al. 2011).

In order to block the flame and particle glow, interference bandpass filters with a central wavelength of 895 nm and a bandwidth of 10 nm are used. Hence, a saturation of the used photodetectors is prevented, but for 895 nm the detectors also receive ambient light from the flame. However, since the fluctuation of the ambient light during one period of the laser frequency modulation is negligible, the flame ambient light causes no systematic error (Fischer et al. 2013a).

3.2.2 Chemiluminescence measurements

In order to localize the reaction zone of the flame and to acquire a measure for the heat release rate of the flame, measurements of the chemiluminescence emission of CH*, OH* or CO_2* can be used according to Lee and Santavicca (2003), Leo et al. (2007). Here, a time-averaged but spatially resolved measurement of the CH* emission and a temporally resolved but spatially averaged measurement of the OH* emission are performed.

The CH* emission is measured using a camera of the type theta system SIS1-s285 equipped with a Thorlabs bandpass filter of the type FGB25S with a central wavelength of 380 nm and with 130 nm full width at half maximum. Note that the integral CH* emission along the line of sight in *y* direction is acquired. Assuming that the flame is rotationally symmetric, the CH* emission in the *x–z* plane for $y = 0$ is calculated from the integral recording using the inverse Abel transform. Hence, a time-averaged measurement of the heat release rate can be performed with only one observation direction.

Furthermore, the OH* emission is recorded using a Thorlabs PMM01 photomultiplier (PM) module equipped with an Edmund optics bandpass filter with a central wavelength of (310 ± 3) nm and a full width at half maximum of (10 ± 2) nm. The PM signal is sampled with a rate of 2 MHz enabling a frequency analysis of the OH* emission.

3.2.3 Sound pressure recording

In order to acquire the sound pressure oscillations in the far-field, a calibrated condenser microphone of the type G.R.A.S 40BP-S1 is used. The analog output of the microphone is recorded using the data acquisition card of the

measurement PC. The microphone is located 20 cm away from the burner axis at the height of the outlet.

4 Results

The following measurements are performed in the region from $z = 4$ mm to $z = 32$ mm with $z = 0$ located at the burner surface. In the white regions with $z > 4$ mm, the velocity values are discarded by a threshold due to low scattered light powers below 0.2 nW.

4.1 Mean velocity values

In order to calculate the swirl number of the flames, the mean velocity values are determined. The mean value of the flow velocity in the x–z plane above the burner outlet for all three velocity components is shown in Fig. 6a, b
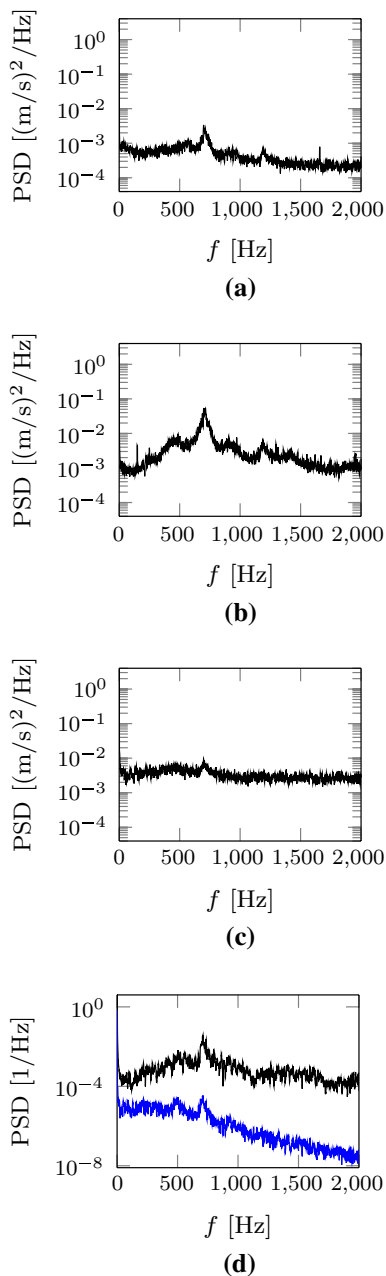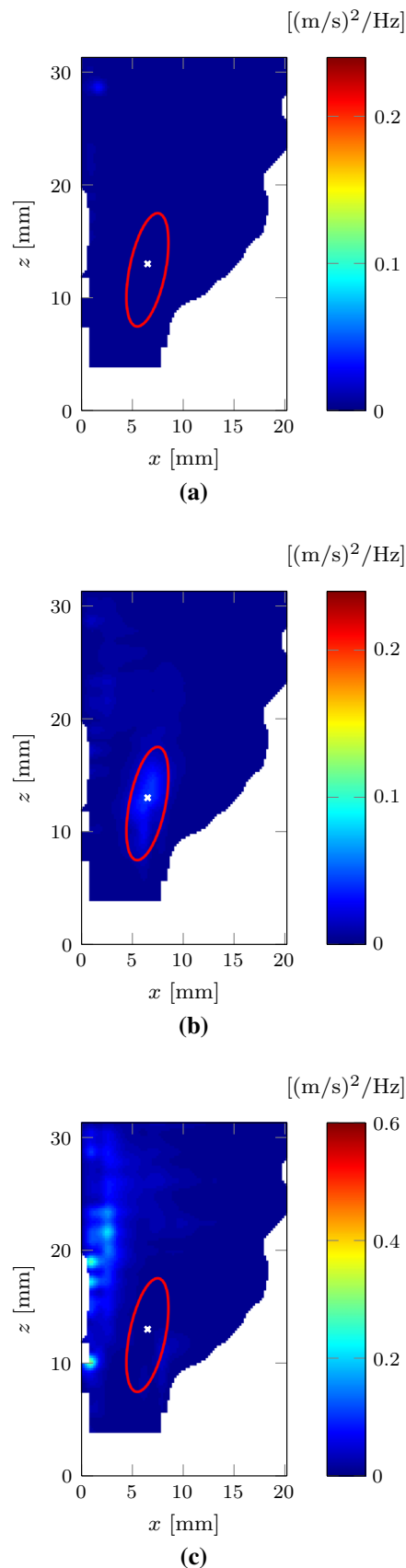

Fig. 7 Power spectral density of **a** the tangential, **b** the radial and **c** the axial flow velocity component and **d** the normalized sound emission (*black*) and OH* emission (*blue*) for the design point
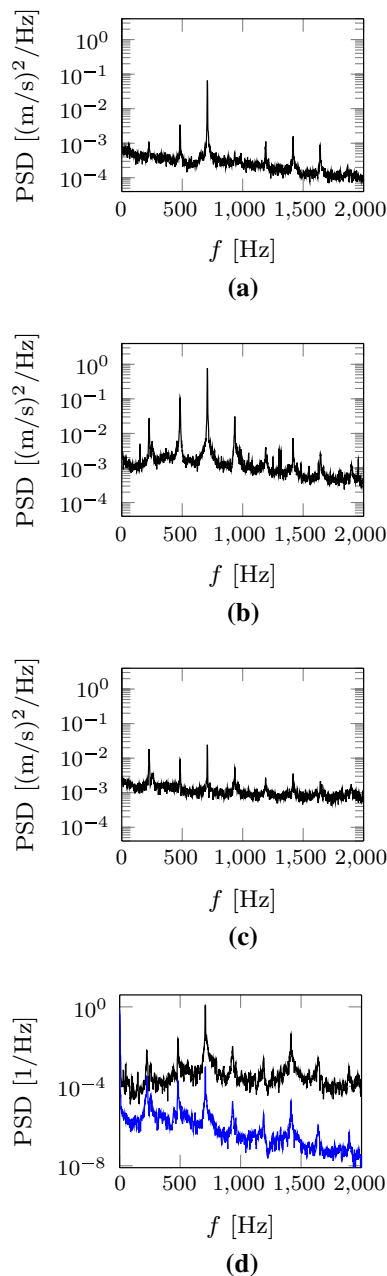
Fig. 8 Power spectral density of **a** the tangential, **b** the radial and **c** the axial flow velocity component and **d** the normalized sound emission (*black*) and OH* emission (*blue*) for the noisy flame
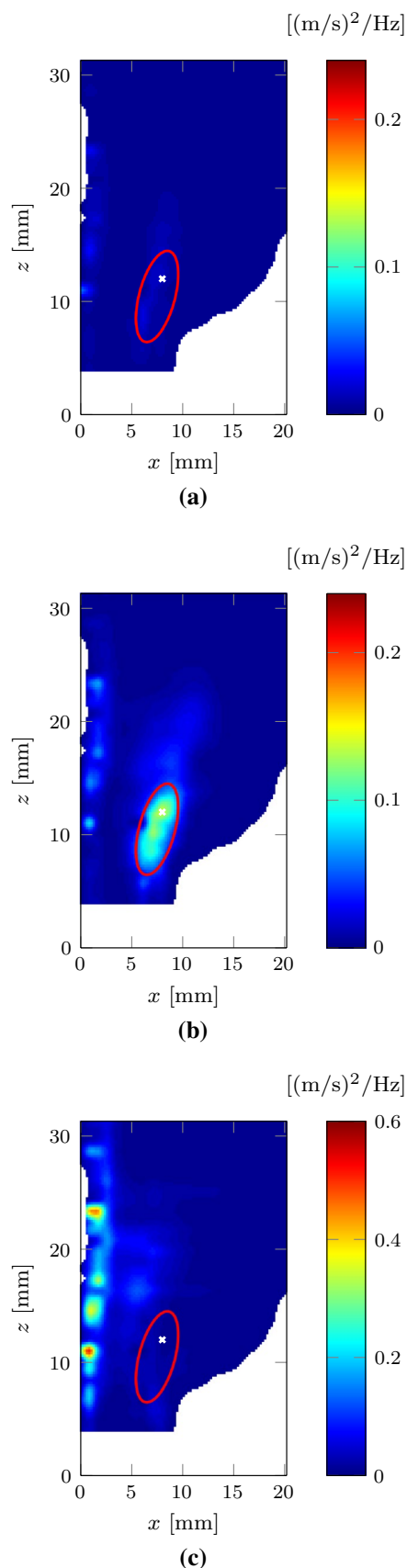
(a)

(b)

(c)

◀ **Fig. 9** Mean value of the power spectral density of the velocity in the range of 700–720 Hz for **a** the tangential, **b** the radial and **c** the axial velocity component of the design point

for the "design point" and the "noisy flame," respectively. The velocity components v_x and v_z are imaged by the vectors; the color depicts the out-of-plane component v_y given a right-handed Cartesian coordinate system. The expected random error is estimated based on the discussion in Sect. 2.3.2 with the measurement duration $T = 10$ s. Hence, it follows a random error of 0.63×10^{-2} m/s for the x and y components and 2.11×10^{-2} m/s for the z component of the velocity for a scattered light power of 0.2 nW in the outer regions of the flame. In the inner flame region, a scattered light power of up to 10 nW occurs, resulting in a random error of 0.06×10^{-2} m/s for the x and y components and 0.19×10^{-2} m/s for the z component. In relation to the mean flow velocity, these values are negligible and no artifacts or deviations due to random errors are visible in Fig. 6.

Both flame shapes appear very similar to the noisy flame being slightly more expanded. For both flames, a flow toward the center of the flame is visible directly above the burner outlet. Starting from a height of 10 mm the flow expands in the radial direction. The exit velocities amount to approximately 8.3 and 7.7 m/s. The resulting swirl number for the design point is 0.38 compared to 0.47 for the noisy flame. Hence, both flames are considered to be in low-swirl condition. As characteristic for low-swirl flames, no back flow at the burner axis is visible (Cheng 1995).

4.2 Velocity, sound and chemiluminescence spectra

In order to demonstrate the coupling between the local velocity oscillations in the near-field and the sound pressure in the far-field, the frequency spectra of the velocity, the sound pressure and the OH* emissions are evaluated. The (one-sided) power spectral densities (PSD) of the velocity for the measurement points with the highest oscillation amplitude are shown for all three components in Figs. 7a–c and 8a–c for the "design point" and the "noisy flame," respectively. The normalized PSD of the global sound pressure and the OH* emission is plotted for comparison reason in Figs. 7d and 8d. Due to the random error of the velocity measurement discussed in Sect. 2.3.2, a systematic deviation and a random error for the PSD of the velocity results. In order to estimate both uncertainty contributions, white Gaussian noise is supposed, which leads to a non-central Chi-squared distribution for the sum of the squared Fourier coefficients (Händel 2010). Given a measurement rate of 10 kHz, the systematic error is calculated to 2×10^{-4} (m/s)^2/Hz for the measurements shown in Figs. 7 and 8. The

$[(m/s)^2/Hz]$

(a)

$[(m/s)^2/Hz]$

(b)

$[(m/s)^2/Hz]$

(c)

◀ **Fig. 10** Mean value of the power spectral density of the velocity in the range of 700–720 Hz for **a** the tangential, **b** the radial and **c** the axial velocity component of the noisy flame

minimum random error of the PSD is estimated to 2×10^{-4} $(m/s)^2/Hz$. In comparison with the measured velocity oscillations of up to 0.8 $(m/s)^2/Hz$, these uncertainty contributions can be neglected.
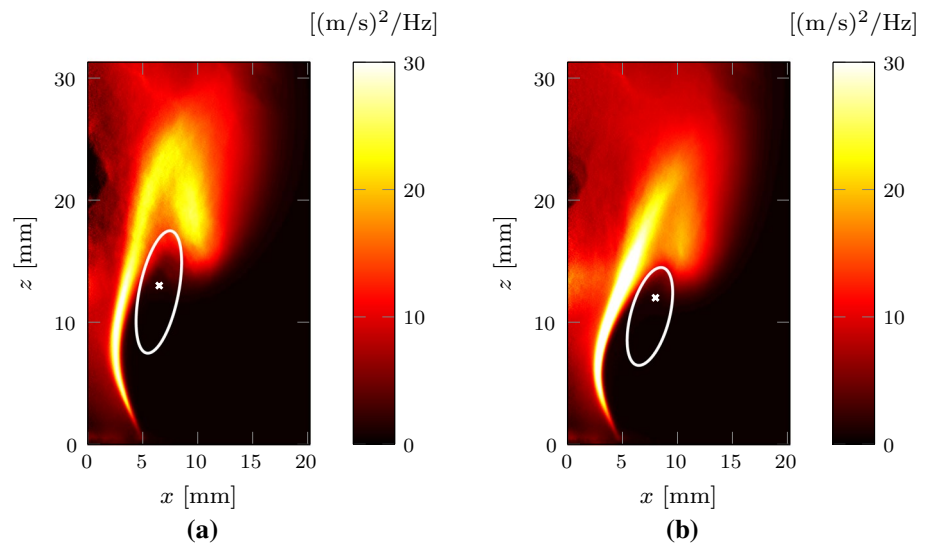
For the design point, only weak velocity oscillations for the radial velocity component in an interval about 708 Hz are visible with a maximum value of 6×10^{-2} $(m/s)^2/Hz$. Other peaks do not occur in the spectrum. Also, the tangential and axial velocities show nearly no oscillation. As expected from the velocity spectra, the sound pressure and OH* emission measurements show a maximum amplitude in the same frequency range around 708 Hz.

For the noisy flame, several peaks in the power spectral density are visible. The strongest oscillation occurs for a frequency of 708 Hz for the radial velocity component with a value of 0.8 $(m/s)^2/Hz$. This is by a factor of 13 higher compared to the design point. Other distinct peaks are found for frequencies of 226, 482, 708, 934, 1190, 1416, 1642 and 1898 Hz. With regard to the difference frequencies of these oscillations, it is assumed that a frequency mixing between the fundamental mode of 226 and 708 Hz and its second harmonic with 1416 Hz occurs. This mixing is also found for the tangential and axial velocity components; however, the oscillation amplitudes are by a factor of 10 or more lower. Again, the sound pressure and OH* emission spectra show distinct peaks at the same frequencies.

These oscillations do not occur in case the flame is not ignited and only air and gas are flowing through the burner. Hence, the reason of the oscillations is a coupling between the combustion and pressure. The local heat release rate is sensitive to fluctuations in the flow field or in the local mixture of the reactants. These fluctuations can be generated by pressure oscillations (Caux-Brisebois et al. 2014; Steinberg et al. 2010). Also, local velocity oscillations in the near-field induce fluctuations of the sound pressure in the far-field.

In order to identify the spatial origin of the sound pressure oscillations within the flame, the mean amplitude of the flow velocity oscillations for the frequency range from 700 to 720 Hz is shown in Figs. 9a–c and 10a–c for the design point and the noisy flame, respectively. Regarding the radial velocity component, the highest amplitudes occur slightly above the position of the highest tangential velocity within a ring of 14 mm diameter around the burner axis (marked in the figure with red ellipses). Further maxima of the oscillation amplitude can be found near the burner axis, especially for the axial velocity component. Given the agreement with the sound pressure spectra, the origin of the sound pressure emission in the near-field can be related to

Fig. 11 Amplitude of the CH* emission (a.u.) for **a** the design point and **b** the noisy flame

these two areas within the flame. Also, the spatial relation of the velocity oscillations to the heat release rate is visualized by means of CH* emission measurement. In Fig. 11, the amplitude of the mean CH* emission is shown for the design point and the noisy flame. The strongest velocity oscillations occur near the outer border of the flame front. Hence, a thermoacoustic coupling of oscillations of the local heat release rate and thereby caused pressure fluctuations is assumed to cause velocity oscillations at the flame front, which result in a significant sound pressure oscillation in the far-field.

4.3 Phase-averaged velocity values

In order to investigate the phasing of the flow velocity oscillations between different positions within the flame, the phase-averaged velocity is calculated using the sound pressure signal recorded by the microphone as a reference. For that purpose, 16 phase slots are chosen and all velocity values associated with the respective slot are averaged. This also reduces the effective measurement duration per phase slot to 0.625 s. The phase-averaged velocity for distinct phase angles of the sound pressure and flow velocity is shown in Figs. 12 and 13 for the design point and the noisy flame for phase angles of 0° and 180° at a frequency of 708 Hz. Similar to Fig. 6, the vectors depict the inplane components v_x and v_z, the color represents the out-of-plane component v_y. For each measurement point, the mean value of the velocity was subtracted in order to highlight the velocity oscillation. Given the measurement duration of 0.625 s, a random error of 2.53×10^{-2} m/s for the x and y components and 8.45×10^{-2} m/s for the z component for a scattered light power of 0.2 nW at the outer region of the flame results. For the inner flame regions, the increased scattered light power of 10 nW leads to a reduced random

error of 0.23×10^{-2} m/s for the x and y components and 0.76×10^{-2} m/s for the z component. Hence, in the inner flame regions, no deviations are visible in Figs. 12 and 13.

In agreement with Figs. 9 and 10, the highest amplitudes occur in the areas marked with the red ellipses. Furthermore, vortex structures of the flow velocity, which are moving in the main flow direction, occur in this area for the noisy flame.

5 Summary and outlook

In this paper, an FM-DGV system capable of performing simultaneous three-component flow velocity measurements in flames was presented for the first time. In order to demonstrate the suitability of the 3C FM-DGV for the investigation of the combustion flow dynamics in a swirl-stabilized flame, combined time-resolved measurements of the flow velocity and the heat release rate in the acoustic near-field and the sound pressure emission in the acoustic far-field were performed. Thereby, the spatial origin of the sound emission of the swirl-stabilized flame was located and oscillations at the same frequency of 708 Hz were found. Hence, a thermoacoustic coupling of the heat release rate, the flow velocity and the pressure was shown in accordance with the literature (Caux-Brisebois et al. 2014) and is assumed to lead to the sound emission in the acoustic far-field. Consequently, the 3C FM-DGV system is a valuable tool for further flow velocity measurements in swirled combustion research.

Given the time-resolved OH* emission Q and flow velocity v, it is in principle possible to calculate the flame transfer function (FTF) $\mathcal{F}$, which is defined as the ratio of the relative heat release rate fluctuations (Q'/Q) to the relative velocity fluctuations (v'/v) (Candel et al. 2014).
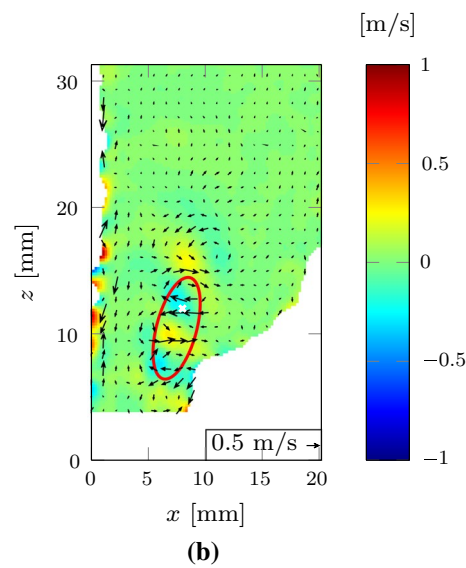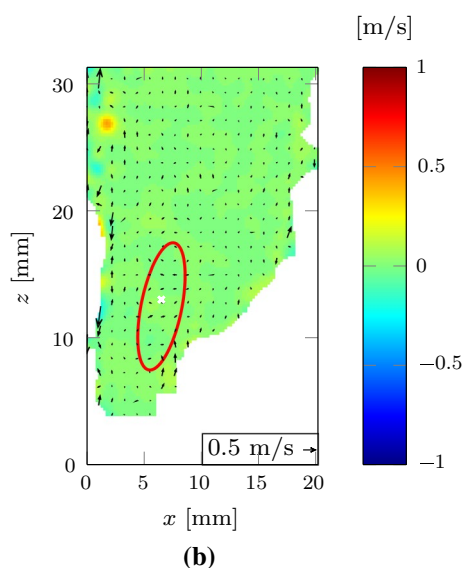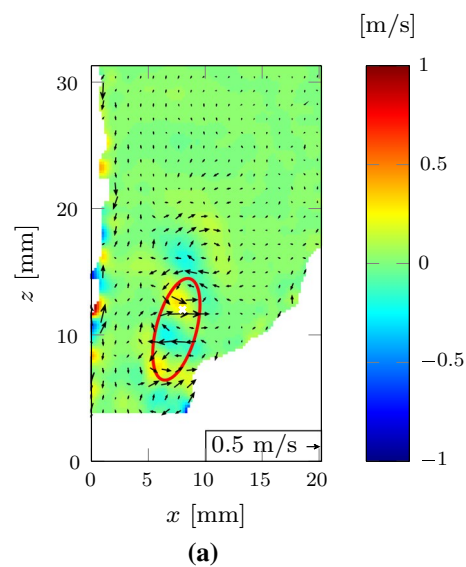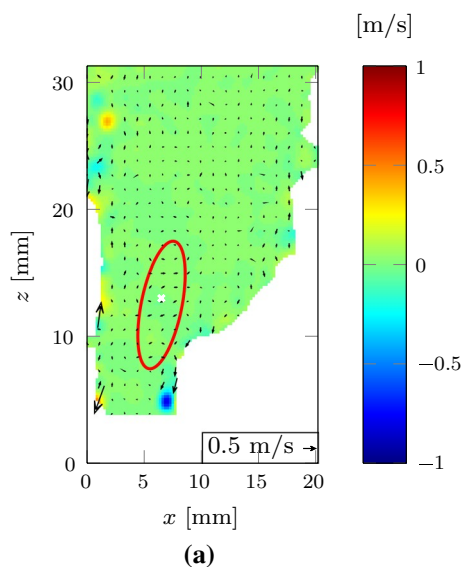
Fig. 12 Phase-averaged flow velocity for a phase angle of **a** 0° and **b** 180° for the design point

Fig. 13 Phase-averaged flow velocity for a phase angle of **a** 0° and **b** 180° for the noisy flame

As this concept is mainly applied to flames with artificial sound excitation, e.g., by a siren, it does not provide further information about the self-excited flame presented here. However, for appropriate flames a spatially resolved FTF for each velocity component could be calculated given the 3C FM-DGV velocity data. These benefits may lead to a deeper understanding of the thermoacoustic coupling with swirl-stabilized, premixed flames. In addition, the high measurement rate and the simultaneous acquisition of all three velocity components in particular allow to investigate unsteady phenomena such as ignition processes. Furthermore, the proposed 3C FM-DGV system is compatible with endoscopic measurement approaches, which enables in situ measurements, e.g., in engines with limited optical access.

References

Alavandi S, Agrawal A (2005) Lean premixed combustion of carbon-monoxide-hydrogen-methane fuel mixtures using porous inert media. In: Proceedings of ASME Turbo Expo 2005, Reno-Tahoe, Nevada, USA, GT2005-68586

Baker R, Hutchinson P, Khalil E, Whitelaw J (1975) Measurements of three velocity components in a model furnace with and without combustion. Fifteenth Symposium (International) on Combustion 15(1):553–559

Boxx I, Arndt CM, Carter CD, Meier W (2012) High-speed laser diagnostics for the study of flame dynamics in a lean premixed gas turbine model combustor. Exp Fluids 52(3):555–567

Boxx I, Carter CD, Stöhr M, Meier W (2013) Study of the mechanisms for flame stabilization in gas turbine model combustors using kHz laser diagnostics. Exp Fluids 54(5):1532

Candel S, Durox D, Schuller T, Bourgouin JF, Moeck JP (2014) Dynamics of swirling flames. Annu Rev Fluid Mech 46:147–173

Caux-Brisebois V, Steinberg AM, Arndt CM, Meier W (2014) Thermo-acoustic velocity coupling in a swirl stabilized gas turbine model combustor. Combust Flame 161(12):3166–3180

Charrett TOH, Tatam RP (2006) Single camera three component planar velocity measurements using two-frequency planar Doppler velocimetry (2v-PDV). Meas Sci Technol 17(5):1194–1206

Charrett TOH, Nobes DS, Tatam RP (2007) Investigation into the selection of viewing configurations for three-component planar Doppler velocimetry measurements. Appl Opt 46(19):4102–4116

Cheng RK (1995) Velocity and scalar characteristics of premixed turbulent flames stabilized by weak swirl. Combust Flame 101:1–14

Fischer A, Büttner L, Czarske J, Eggert M, Grosche G, Müller H (2007) Investigation of time-resolved single detector Doppler global velocimetry using sinusoidal laser frequency modulation. Meas Sci Technol 18(8):2529–2545

Fischer A, Büttner L, Czarske J, Eggert M, Müller H (2008a) Measurement uncertainty and temporal resolution of Doppler global velocimetry using laser frequency modulation. Appl Opt 47(21):3941–3953

Fischer A, König J, Czarske J (2008b) Speckle noise influence on measuring turbulence spectra using time-resolved Doppler global velocimetry with laser frequency modulation. Meas Sci Technol 19(12):125402

Fischer A, Büttner L, Czarske J, Eggert M, Müller H (2009) Measurements of velocity spectra using time-resolving Doppler global velocimetry with laser frequency modulation and a detector array. Exp Fluids 47(4–5):599–611

Fischer A, Büttner L, Czarske J (2011a) Simultaneous measurements of multiple flow velocity components using frequency modulated lasers and a single molecular absorption cell. Opt Commun 284(12):3060–3064

Fischer A, Haufe D, Büttner L, Czarske J (2011b) Scattering effects at nearwall flow measurements using Doppler global velocimetry. Appl Opt 50:4068–4082

Fischer A, König J, Czarske J, Peterleithner J, Woisetschläger J, Leitgeb T (2013a) Analysis of flow and density oscillations in a swirl-stabilized flame employing highly resolving optical measurement techniques. Exp Fluids 54:1622

Fischer A, König J, Haufe D, Schlüßler R, Büttner L, Czarske J (2013b) Optical multi-point measurements of the sound particle velocity with frequency modulated Doppler global velocimetry. J Acoust Soc Am 134(2):1102–1111

Giezendanner R, Keck O, Weigand P, Meier W, Meier U, Stricker W, Aigner M (2003) Periodic combustion instabilities in a swirl burner studied by phase-locked planar laser-induced fluorescence. Combust Sci Technol 175(4):721–741

Giuliani F, Wagner B, Woisetschläger J, Heitmeir F (2006) Laser vibrometry for real-time combustion stability diagnostic. In: ASME Turbo Expo 2006

Giuliani F, Leitgeb T, Lang A, Woisetschläger J (2010) Mapping the density fluctuations in a pulsed air-methane flame using laser-vibrometry. J Eng Gas Turbines Power 132(3):031,603

Giuliani F, Woisetschläger J, Leitgeb T (2012) Design and validation of a burner with variable geometry for extended combustion range. In: Proceedings of ASME Turbo Expo, Copenhagen, Denmark., GT2012-68236

Gounder JD, Boxx I, Kutne P, Wysocki S, Biagioli F (2014) Phase resolved analysis of flame structure in lean premixed swirl flames of a fuel staged gas turbine model combustor. Combust Sci Technol 186(4–5):421–434

Haufe D, Fischer A, Czarske J, Schulz A, Bake F, Enghardt L (2013) Multi-scale measurement of acoustic particle velocity and flow velocity for liner investigations. Exp Fluids 54:1569

Henning A, Kaepernick K, Ehrenfried K, Koop L, Dillmann A (2008) Investigation of aeroacoustic noise generation by simultaneous particle image velocimetry and microphone measurements. Exp Fluids 45(6):1073–1085

Händel P (2010) Amplitude estimation using IEEE-STD-1057 three-parameter sine wave fit: statistical distribution, bias and variance. Measurement 43(6):766–770

Komine H, Brosnan SJ, Stappaerts E (1991) Real-time, Doppler global velocimetry. In: AIAA 29th Aerospace Sciences Meeting, Reno (Nevada), AIAA-91-0337

Lee JG, Santavicca DA (2003) Experimental diagnostics for the study of combustion instabilities in lean premixed combustors. J Propul Power 19(5):735–750

Leo MD, Saveliev A, Kennedy LA, Zelepouga SA (2007) OH and CH luminescence in opposed flow methane oxy-flames. Combust Flame 149(4):435–447

Lilley DG (1977) Swirl flows in combustion: a review. AIAA J 15(8):1063–1078

Meadows J, Agrawal AK (2014) Time-resolved PIV measurements of non-reacting flow field in a swirl-stabilized combustor without and with porous inserts for acoustic control. In: Proceedings of ASME Turbo Expo, GT2014-27203

Meyers JF (1995) Development of Doppler global velocimetry as a flow diagnostics tool. Meas Sci Technol 6(6):769–783

Müller H, Eggert M, Czarske J, Büttner L, Fischer A (2007) Single-camera Doppler global velocimetry based on frequency modulation techniques. Exp Fluids 43(2–3):223–232

Röhle I, Willert CE (2001) Extension of Doppler global velocimetry to periodic flows. Meas Sci Technol 12(4):420–431

Richards G, McMillian M, Gemmen R, Rogers W, Cully S (2001) Issues for low-emission, fuel-flexible power systems. Prog Energy Combust Sci 27:141–169

Sadanandan R, Stöhr M, Meier W (2009) Flowfield–flame structure interactions in an oscillating swirl flame. Combust Explos Shock Waves 45(5):518–529

Schlüßler R, Czarske J, Fischer A (2014) Uncertainty of flow velocity measurements due to refractive index fluctuations. Opt Lasers Eng 54:93–104

Self SA, Whitelaw JH (1976) Laser anemometry for combustion research. Combust Sci Technol 13(1–6):171–197

Steinberg A, Boxx I, Stöhr M, Carter C, Meier W (2010) Flow–flame interactions causing acoustically coupled heat release fluctuations in a thermo-acoustically unstable gas turbine model combustor. Combust Flame 157(12):2250–2266

Stöhr M, Boxx I, Carter CD, Meier W (2012) Experimental study of vortex–flame interaction in a gas turbine model combustor. Combust Flame 159(8):2636–2649

Syred N (2011) 40 years with swirl, vortex, cyclonic flows, and combustion. In: Aerospace Sciences Meetings, American Institute of Aeronautics and Astronautics

Syred N, Beér J (1974) Combustion in swirling flows: a review. Combust Flame 23(2):143–201

Syred N, Chigier N, Beér J (1971) Flame stabilization in recirculation zones of jets with swirl. Thirteenth symposium (International) on Combustion 13(1):617–624

Yilmaz İlker, Ratner A, Ilbas M, Huang Y (2010) Experimental investigation of thermoacoustic coupling using blended hydrogen-methane fuels in a low swirl burner. Int J Hydrog Energy 35(1):329–336